Astronomy & Astrophysics manuscript no. aanda
April 13, 2026

GLIMPSED: Direct evidence for a fast AGN-driven outflow from a $z = 6.64$ Little Red Dot host galaxy

Damien Korber[1⋆], Rui Marques-Chaves[1], Daniel Schaerer[1, 2], Gabriel Brammer[3], Archana Aravindan[4, 5], Arghyadeep Basu[6], Qinyue Fei[7], Emma Giovinazzo[1], Vasily Kokorev[4], Alberto Saldana-Lopez[8], Maxime Trebitsch[9], Hakim Atek[10], John Chisholm[4, 5], Ryan Endsley[4], Seiji Fujimoto[7, 11], Lukas Furtak[4, 5], Richard Pan[12], and Rohan P. Naidu[13]

1 Observatoire de Genève, Université de Genève, Chemin Pegasi 51, 1290 Versoix, Switzerland
2 CNRS, IRAP, 14 Avenue E. Belin, 31400 Toulouse, France
3 Cosmic Dawn Center (DAWN), Niels Bohr Institute, University of Copenhagen, Jagtvej 128, København N, DK-2200, Denmark
4 Department of Astronomy, The University of Texas at Austin, Austin, TX 78712, USA
5 Cosmic Frontier Center, The University of Texas at Austin, Austin, TX 78712, USA
6 Univ Lyon, Univ Lyon1, Ens de Lyon, CNRS, CRAL UMR5574, F-69230, Saint-Genis-Laval, France
7 David A. Dunlap Department of Astronomy and Astrophysics, University of Toronto, 50 St. George Street, Toronto, Ontario, M5S 3H4, Canada
8 Department of Astronomy, Oskar Klein Centre, Stockholm University, 106 91 Stockholm, Sweden
9 LUX, Observatoire de Paris, Université PSL, Sorbonne Université, CNRS, 75014 Paris, France
10 Institut d'Astrophysique de Paris, UMR 7095, CNRS, Sorbonne Université, 98 bis boulevard Arago, 75014 Paris, France
11 Dunlap Institute for Astronomy and Astrophysics, University of Toronto, Toronto, ON M5S 3H4, Canada
12 Department of Physics & Astronomy, Tufts University, MA 02155, USA20
13 MIT Kavli Institute for Astrophysics and Space Research, 70 Vassar Street, Cambridge, MA 02139, USA

Received MONTH DAY, YEAR; accepted MONTH DAY, YEAR

ABSTRACT

We report the discovery of GLIMPSED-329380, a $z = 6.64$ galaxy behind Abell S1063, which shows signs of an extreme ionised outflow driven by an active galactic nucleus (AGN). The deep JWST/NIRSpec medium grating observations show spatially resolved structures of a host galaxy containing the very fast outflow and an AGN, which we analyse separately. The outflow, mainly traced by broad [O iii]$\lambda\lambda$4960,5008 and Hα emissions in the host, reaches a full-width half-maximum velocity of $\sim$ 5500km s^{-1}, velocities only observed in AGN-dominated systems. From the Balmer decrement, we observe that while the narrow emission lines show no dust attenuation, the outflowing gas is dusty. We use emission lines diagnostics to infer gas abundances within the host galaxy. The oxygen abundance is 12 + log(O/H) $\sim$ 7.95 ($\sim$ 18% solar) and the host is slightly nitrogen-enriched with log(N/O) ~ -0.75. Despite its extreme velocity, the mass loading factor (< 0.1) and the kinematic energy of the outflow ($\sim 10^{43}$erg s^{-1}) suggest limited impact on star formation. The AGN component shows many similarities with little red dots (LRDs): a characteristic "V-shape", exponential profile in hydrogen lines, numerous detection of forbidden [Fe ii] lines, a Balmer break, and a broad absorption feature at $\sim$ 4550 Å. This detection of a fast outflow in an LRD, rare in surveys dominated by low-resolution (e.g. PRISM) spectra, provides direct evidence of AGN activity in these systems.

Key words. some keywords – separated by two dash lines

1. Introduction

Outflows are a fundamental mechanism for regulating galaxy evolution, driven by processes acting across different scales. On local scales, starburst activity powers outflows with velocities of hundreds of km s^{-1} (e.g. Arribas et al. 2014; Förster Schreiber et al. 2019; Roberts-Borsani et al. 2020; Llerena et al. 2023; Saldana-Lopez et al. 2025; Rodríguez Del Pino et al. 2026), shaping the interstellar medium and disturbing star formation (e.g. Hopkins et al. 2014). In the early Universe, such feedback may contribute to the bursty star formation histories observed in high-redshift galaxies (e.g. Endsley et al. 2024). On larger scales, accreting supermassive black holes in active galactic nuclei (AGN) drive far more energetic outflows, reaching velocities up to several thousand km s^{-1} (e.g. Arribas et al. 2014; King & Pounds 2015; Förster Schreiber et al. 2019; Bertola et al. 2025; Nandi et al. 2026). AGN-driven outflows can disrupt the galaxy gas reservoir on a larger scale, potentially quenching star formation (e.g. Förster Schreiber et al. 2019; Veilleux et al. 2020; Cooper et al. 2025). By tracing the kinematics and physical conditions of outflowing gas, we gain insights into the energy sources powering them and their impact on galaxy growth.

The James Webb Space Telescope has revealed in the last years a new category of objects called Little Red Dots (LRDs, Matthee et al. 2024). These objects were identified as red, unresolved dots in JWST/NIRCam observations, showing an V-shaped SED and broad Balmer emission lines (e.g. Matthee et al. 2024; Furtak et al. 2024; Greene et al. 2024). These objects have gained a lot of attention in the past years and have been studied in many different ways, revealing common properties. These objects potentially contain high density gas en-

⋆ Corresponding author: Damien Korber: damien.korber@protonmail.ch

velopes, as shown by the presence of exponential wings, non-stellar Balmer breaks as well as frequent Balmer absorption features (e.g. Juodžbalis et al. 2024; Ji et al. 2025; D'Eugenio et al. 2025; Lambrides et al. 2025; Ji et al. 2026; Lin et al. 2026; Rusakov et al. 2026). Furthermore, deep enough observations or stack of these objects often reveals the presence of forbidden and permitted [Fe ii] lines (e.g. Lambrides et al. 2025; D'Eugenio et al. 2025; Kokorev et al. 2025; Torralba et al. 2025; Lin et al. 2026; Pérez-González et al. 2026). Their origin remains unclear to date, with some authors suggesting the presence of a black hole surrounded by a gas envelope (e.g. Inayoshi & Maiolino 2025; Kokorev et al. 2025; de Graaff et al. 2025b; Naidu et al. 2025; Kido et al. 2025). This gas would be heated by the black hole, which then radiates black body radiations, hence the observed black-body shaped SED (e.g. de Graaff et al. 2025b; Sun et al. 2026).

While outflows are not a defining feature of LRDs, a growing number of studies report their presence in these systems. Cooper et al. (2025) identified an ionised outflow in an $z \sim 7.04$ LRD from Rinaldi et al. (2025). In their sample, this object exhibits the fastest outflow at $z > 5$, with velocities reaching $v_{\rm out} \sim 758$km s^{-1}. The authors report a companion for this LRD, which could then enhance the outflow due to merging activities (Cooper et al. 2025). D'Eugenio et al. (2026) identified a broad but relatively faint component in [O iii]λ5008 reaching $v_{\rm out} \sim 300$km s^{-1} in a $z \sim 5$ LRD. At lower redshift ($z \sim 0.4$), Chen et al. (2026) reported an extreme ionised outflow reaching $v_{\rm out} \sim 2070$km s^{-1}, in a LRD-like galaxy.

Intuitively, if LRDs host actively accreting black holes, one might expect feedback-driven outflows. However, such outflows are only rarely observed. Recent scenarios propose that a dense gas envelope surrounding the black hole could explain this apparent discrepancy (Inayoshi & Maiolino 2025; de Graaff et al. 2025b; Naidu et al. 2025; Kokorev et al. 2025; Kido et al. 2025; Taylor et al. 2025). In these models, gas accelerated by accretion is confined within the envelope, and its energy is reprocessed into radiation (Kido et al. 2025), producing the observed black-body spectrum (de Graaff et al. 2025b; Naidu et al. 2025). Hence, outflows may only emerge if the envelope becomes unstable, allowing some gas to escape.

In this paper, we present GLIMPSED-329380, a $z = 6.64$ galaxy showing signs of an extreme outflow, alongside a compact AGN exhibiting typical LRD features. This galaxy was initially observed as a filler of the deep medium band GLIMPSE-D survey (DD-9223: Fujimoto et al. 2025). We will present this emission lines-rich spectrum, which can be separated in two components due to being resolved in the 2D spectrum (Sect. 2.1) as well as the limited photometric observations (Sect. 2.2). We then detail the fitting methods (Sect. 2.3 and 2.4). The results are then presented separately for the two components, starting with the host component which presents the extreme outflow (Sect. 3.1) and then the AGN component, describing the different features visible in the spectrum (Sect. 3.2). Finally we discuss the different LRD-like features, which tell us this object is an LRD (Sect. 4.1), then we discuss the outflow in the context of LRDs (Sect. 4.2). We considered a flat ΛCDM cosmology with $H_0 = 70$ km s^{-1} Mpc^{-1}, $\Omega_M = 0.3$, and $\Omega_\Lambda = 0.7$.

2. Data and line measurements

2.1. Spectroscopy

GLIMPSED-329380 lies on the outskirts of the Abell S1063 galaxy cluster (Ra=342.229976deg, Dec=-44.510380deg). This galaxy was observed for 9 hrs with the G395M medium-resolution spectroscopy of *JWST*/NIRSpec, as part of the GLIMPSE-D survey (DDT-9223; Fujimoto et al. 2025). We initially reduced the spectrum using the standard `msaexp` pipeline (Brammer 2023), but due to over-subtraction around the [O iii] wings (as the galaxy is resolved in the 2D spectrum), we adopted an alternative reduction using a global sky subtraction. The general approach to remove the diffuse sky component from the MSA spectra is to take 2D image differences of exposures taken with spatial "nod" offsets of the telescope. With the small 5-pixel (~0.″5) nods necessary to keep the target in the 3-shutter MSA slitlet in all exposures, this can result in "self subtraction" in the outer profiles of extended sources. [1] `msaexp` (Brammer 2023) estimates the 1D spectrum of the sky of a particular exposure from all of the slitlets in an MSA configuration using the portions of the spectra excluding the expected traces of the sources within the slitlets. We adopt a "global" sky subtraction approach by foregoing the nod differences and subtract this 1D sky spectrum from the slit 2D spectra before the combination and rectification of the final spectrum. This technique was previously used in other surveys (de Graaff et al. 2025a) and, unless stated otherwise, the results will assume the global sky noise reduction for the spectra. We extracted the 1D spectrum from the 2D spectrum using msaexp (Brammer 2023). For continuum analysis, we used the standard nod difference reduction, but for emission lines, we used the sky noise reduction to mitigate the over-subtractions, accepting some background patterns at the spectral edges.

The spectrum of GLIMPSED-329380 reveals two spatially distinct components. The first one, hereafter referred to as the AGN component, features a well-detected compact continuum confined to a single pixel and exhibits broad Hα emission, hence its AGN classification. The second one, the host component, displays a much fainter but detected extended continuum, alongside broadened [O iii] emission in the extended regions. We extracted both components separately using the standard drizzled msaexp extraction (Brammer 2023). The two separate spectra can be visualised in Fig. 1, alongside identified emission lines. In addition, we show in Fig. 2 the collapsed spectrum (the sum along the frequency axis), illustrating the extent of the galaxy in the JWST/NIRSpec slit, and the 2D spectrum focused around [O iii]λ5008 with its outflowing component on top and Hα with its broad line region (BLR) and broad component. The full 2D spectrum shows the unresolved AGN, as well as wings corresponding to the contribution of the host. The restricted sum around [O iii] is spatially offset from the AGN, and shows that oxygen lines spread over several kpc.

2.2. Photometry

While GLIMPSED-329380 is located near the Abell S1063 galaxy cluster, it lies just outside the photometric footprint of the ultra-deep GLIMPSE survey (GO-3293; Atek et al. 2025) and was not covered by other JWST surveys. However, the galaxy was detected in several earlier photometric surveys. From space, the BUFFALO HST survey (HST-15117; Steinhardt et al. 2020) observed this galaxy in five *HST*/WFC3 restframe optical filters (F606W, F814W, F105W, F125W, F160W) with a long exposure time (16hrs to 67hrs, F814W being the deepest). As F606W and F814W are beyond lyman-break, the galaxy is only observed in the three red filters. It is also observed in *SPITZER*/IRAC1-

[1] The variance of the differenced exposures is also increased by a factor of $1/N_b$, where N_b is the number of exposures used to define the source-free "sky" and $N_b = 8$ here.

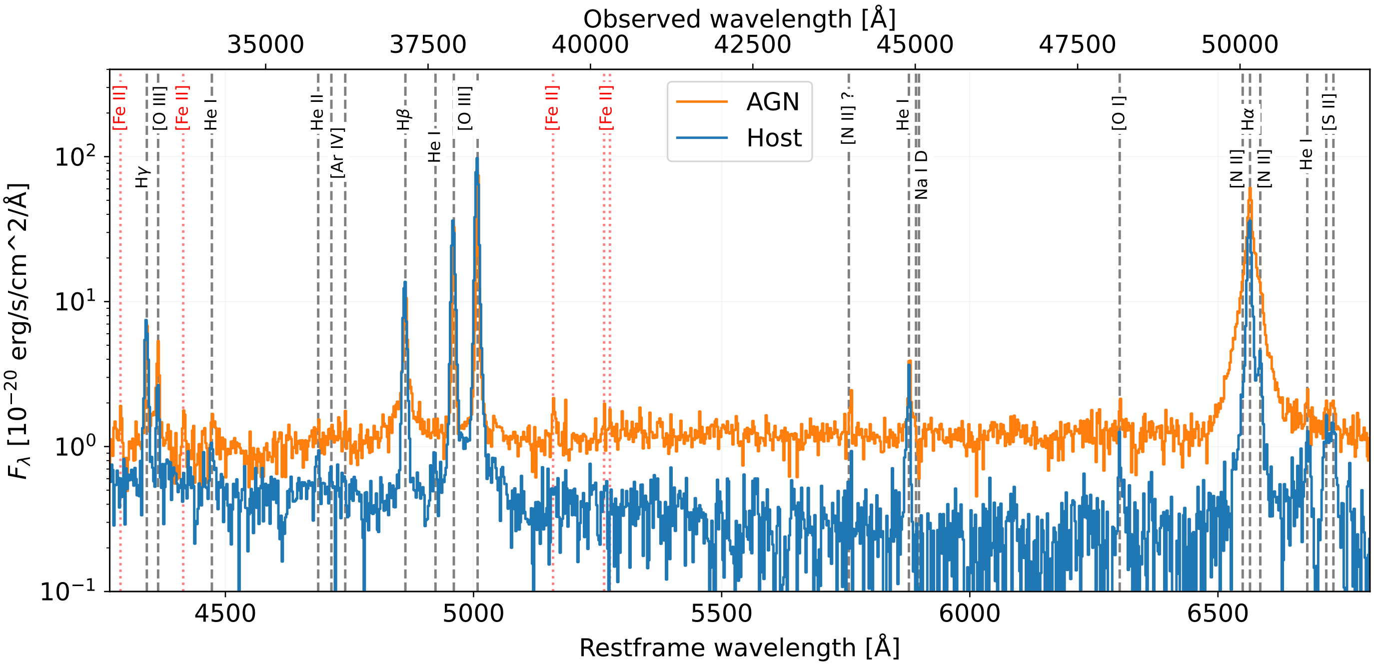

Fig. 1: Separated spectra of the AGN (orange) and host (blue) components with the global noise reduction. The spectrum is restricted to highlight the strong lines.

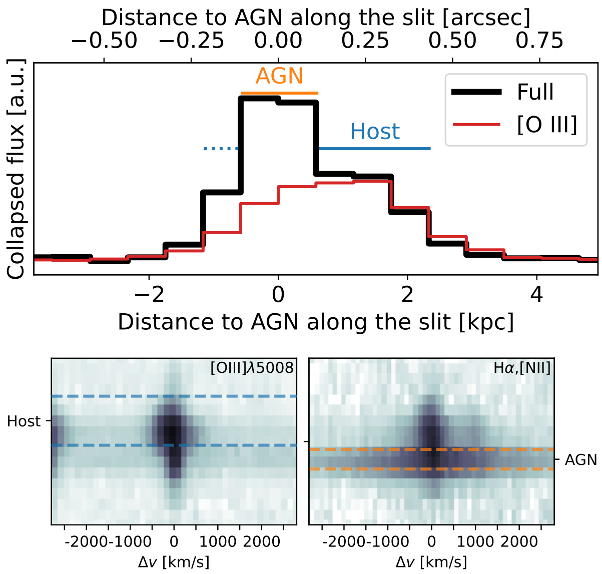

Fig. 2: Top panel: Sum of the flux along frequencies for the full spectrum and the [O III] region. Bottom panel: The 2D spectrum showing [O III]λ5008 and Hα.

4, but is only detected in IRAC1 and 2 (PID-83). From the ground, the KIFF survey (Brammer et al. 2016) detected it with the *VLT*/HAWK-I Ks filter with a long exposure time (22hrs). Interestingly, the non-detections in IRAC3 and IRAC4 suggest the absence of a heavily obscured AGN, which would otherwise be more prominently detected at longer wavelengths. To our knowledge, these are all the available photometric detections, which significantly limits its morphological study. Cutouts of this galaxy are displayed in Fig. 3.

2.3. Modelling the host component

The host component is particularly interesting for the presence of strong outflowing components. In order to characterise the host and its outflows, we fitted the object in four regions of interest: The regions surrounding [O II]$\lambda\lambda$3727,3730, Hγ+[O III]λ4363, Hβ+[O III]$\lambda\lambda$4960,5008 and Hα+[N II]$\lambda\lambda$6550,6585+[S II]$\lambda\lambda$6718,6733.

We first fitted the continuum in each spectral region using a linear fit of the surrounding continuum, except for [O II], for which we used a second degree polynomial due to increased systematic effects at the spectral edges. We subtract the continuum from the spectrum to more easily fit the emission lines. We then modelled separately each emission line using one narrow Gaussian, and for some broader lines, one or two outflow broad components. To limit the number of fit parameters we use several physical considerations. The position of each line is fixed to the restframe wavelength, and is redshifted using the systemic redshift z. For each broad component (called outflow 0 and 1 in the following), we choose one common redshift respectively. We therefore reduced the number of parameters for all emission lines to 3 redshift parameters. For the narrow lines, the width is fixed (in Å), as the lines are unresolved. For each outflow component we assume a constant FWHM (in km s^{-1}), as the broadening exceeds by far the instrumental resolution. This reduces the number of width parameters to 3 as well. Finally, the amplitude of each emission line is kept free, unless fixed by atomic physics. This is the case for [O III]λ5008/[O III]λ4960 = 2.98 (Storey & Zeippen 2000) and [N II]λ6585/[N II]λ6550 = 2.96 (Storey & Zeippen 2000), for which only one amplitude was free. We then used `LMFIT` (Newville et al. 2025) to optimise the parameters. The measured line fluxes of the narrow and broad components (if present) of the host are reported in Table A.1. The emission line fits can be visualised in Fig. 4.

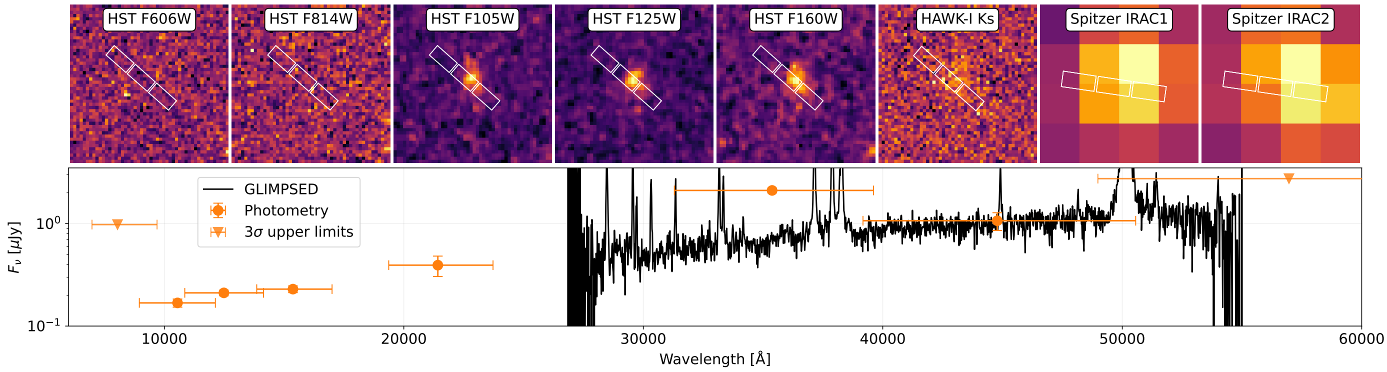

Fig. 3: top panel: Cutout of the available photometry. GLIMPSED-329380 is not detected in F606W and F814W due to the redshift, but is detected in the other filters. The cutout have square sides of 3 arcsec, and the MSA slit is displayed on top of all the images in white. Bottom panel: comparison between the available photometry and the full GLIMPSE-D spectrum (not corrected for slit loss)

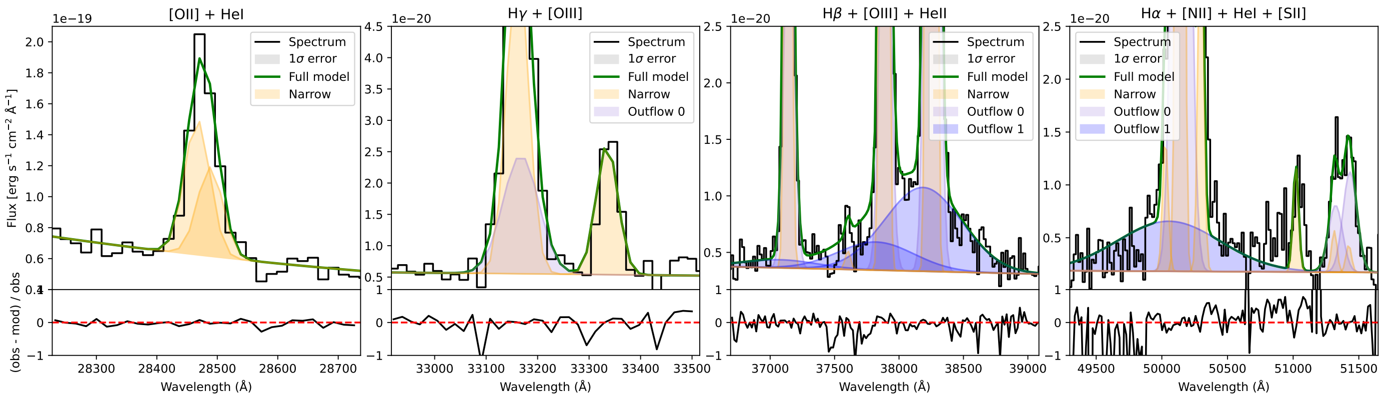

Fig. 4: Top panel: Best fit of the strong emission lines in the host, with the narrow and the broad components. Bottom panel: Residual between of the total fit (green) and the data (black)

2.4. Modelling the AGN component

For the AGN component, we report all the emission lines observed in the spectrum. Due to the large amount of emission lines observed in that component, we opt for a semi-automated modelling of the continuum, with manual selection of the fitting regions for strong emission lines. We first excluded a region of 300Å around the emission lines considered in the model (as tabulated in Tables A.2 and A.3). In these regions, we assume the continuum to be linear. As broad lines span regions larger than 300Å, we enforce a linear continuum as well. These regions are Hγ+[O iii]λ4363, Hβ+[O iii]λλ4960,5008 and Hα+[N ii]λλ6550,6585+[S ii]λλ6718,6733. We then use the median filter from `Scipy` (Virtanen et al. 2020), with a kernel size of 51 pixels, to obtain an estimation of the continuum, which is subtracted from the spectrum to improve fitting.

We use a similar method as the host galaxy to fit the emission lines. The main differences are the number of outflowing components and the fitting of the BLR. In the AGN spectrum, only one broad Gaussian outflow component is observed in [O iii], probably due to the contamination from the host. We included the same velocity Gaussian component in [O iii]λ4363and Hα. In order to fit the BLR wings, we tried to fit both a Gaussian and an exponential. We observe a slightly better fitting with the exponential model (ΔBIC ∼ 59), so we use it for the final fit. While the redshift of the outflow is still free, the redshift of the BLR is fixed to the systemics as we do not expect variation in redshift. All the lines considered for the AGN are reported in Table A.2, except for forbidden iron lines reported in Table A.3. All the fits can be visualised in Fig.5.

3. Results

3.1. Host galaxy properties

Using the method described earlier, we find that most of our emission lines are well fitted by a single narrow line component. For the strongest lines (Hγ, Hβ, [O iii]λλ4960,5008, Hα and [S ii]λλ6718,6733), the addition of one or two broad components strongly improves the fit of the wings. Most of these lines only require one broader component of $v_{\rm FWHM}$ ∼ 740km s^{-1}, but [O iii] and Hα exhibit an additional extremely large wings which is fitted with a second broader component of $v_{\rm FWHM}$ ∼ 5500km s^{-1}. These broad components can be visualised in Fig. 4. The latter is extreme and is unlikely to be related to the virial motion of the gas. It is consistent with a strong ionised outflow driven by an AGN. Therefore, we will consider from now on that these broad components represent ionised outflowing gas.

3.1.1. Dust attenuation in the outflow

In Table A.1, we report significant (∼ 7σ) detection of outflows in successive Balmer series emission lines. In the absence of dust, galaxies are expected to follow ratios of Hα/Hβ = 2.69 and Hβ/Hγ = 2.06, assuming case B recombination and T_e = 20000K (close to the T_e measurement from Sect. 3.1.2)

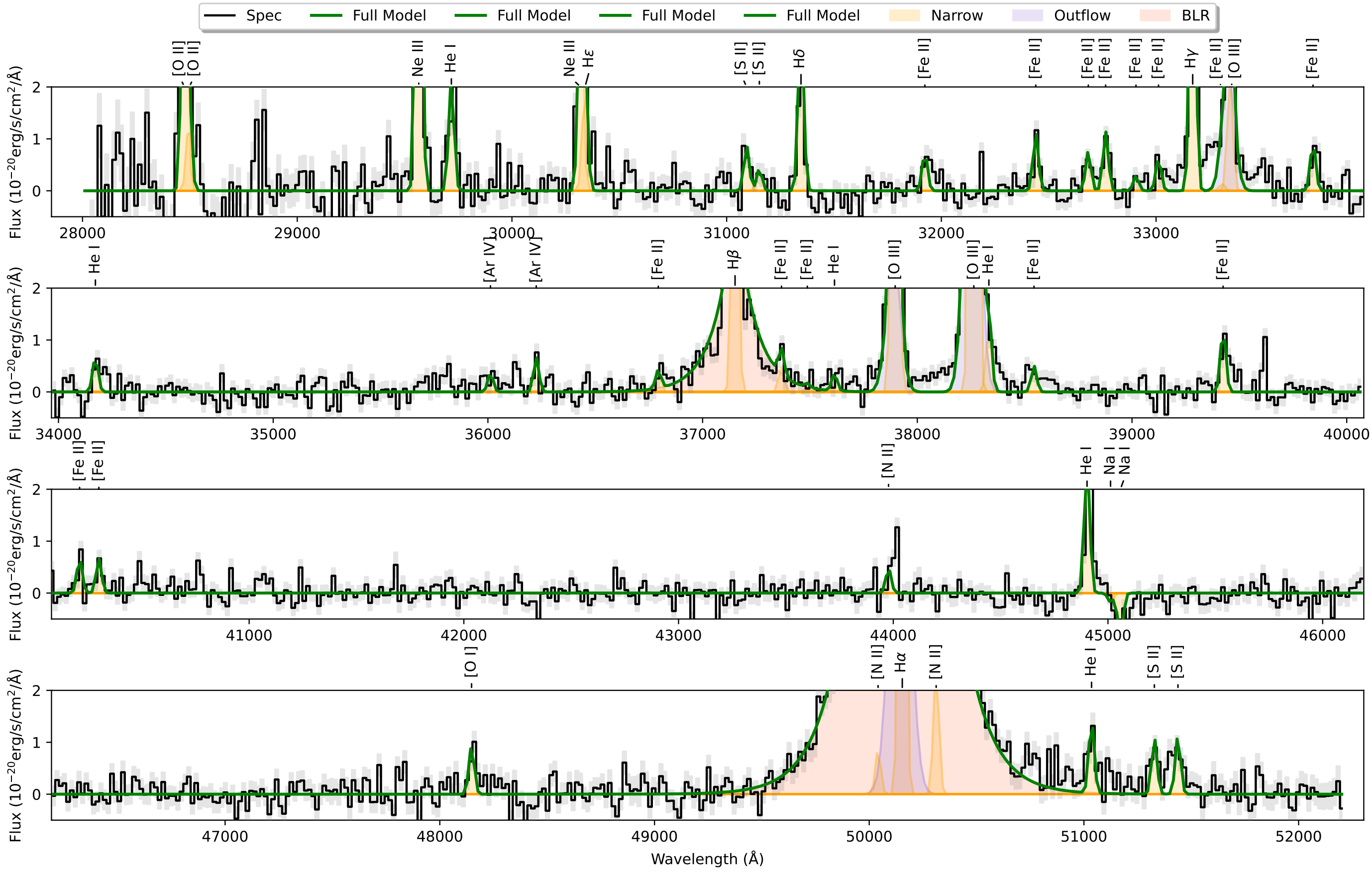

Fig. 5: Background subtracted spectrum of the AGN component. This figure includes the fit of emission lines that are found in Table A.2. The location of the [Fe II] lines are highlighted by red vertical lines.

(Osterbrock & Ferland 2006). Our narrow line analysis yields a ratio of $\mathrm{H}\alpha/\mathrm{H}\beta = 2.72 \pm 0.22$ and $\mathrm{H}\beta/\mathrm{H}\gamma = 1.96 \pm 0.31$. Then, the first outflow component yields $\mathrm{H}\alpha/\mathrm{H}\beta = 4.32 \pm 0.80$ and $\mathrm{H}\beta/\mathrm{H}\gamma = 2.02 \pm 0.68$, and the faster outflow component yields $\mathrm{H}\alpha/\mathrm{H}\beta > 3.32$ due to the Hβ flux upper limit. The narrow component is thus compatible with case B recombination, indicating minimal dust attenuation. In contrast, the outflows show evidence of dust. The Balmer decrement (Hα/Hβ) of the first outflow deviates from case B, indicating significant attenuation. For the second outflow, only a lower limit is measured, which is already redder than case B. We note a slight inconsistency in the attenuation inferred with the second tracer (Hβ/Hγ) in the first outflow. Under larger uncertainties, it suggests minimal attenuation. However, due to the weakness of Hγ and the strong attenuation indicated by the Balmer decrement, we do not expect to observe a significant outflowing component in Hγ. In this picture, we expect the dust within the host galaxy to be ejected alongside the outflowing ionised gas, which matches recent observations of dusty outflows (Marques-Chaves et al. 2025; Crespo Gómez et al. 2025; Rodríguez Del Pino et al. 2026). In the rest of the results, the dust corrected emission lines from the host component will assume the Cardelli et al. (1989) extinction curve with an attenuation of $E(B-V)_l = 1.48$ for the first outflow and $E(B-V)_l > 0.66$ for the fast outflow. The narrow lines are not corrected for dust.

3.1.2. Electron temperature, electron density and abundances of the host

The electron temperature T_e and density n_e can be estimated using ratios of emission lines sensitive to these quantities. To estimate T_e, we can use the direct method from the ratio of [O III]λ4363and [O III]λ5008 (Sanders et al. 2025), and for n_e, we use the [S II]$\lambda\lambda$6718,6733 doublet (Kewley et al. 2019). In GLIMPSED-329380, the [S II]$\lambda\lambda$6718,6733 doublet is detected, but is affected by the outflow, as shown by the clear broadening in Fig. 4. Hence, we consider the total flux of [S II] to estimate the electron density. In principle, n_e and T_e diagnostics are interdependent, and we need to fit them together. In practice, the uncertainties on [S II]$\lambda\lambda$6718,6733 flux do not properly constrain n_e with a fit. Therefore, we fit T_e with full flux uncertainties, but fix the [S II]$\lambda\lambda$6718,6733 ratio to constrain n_e. We do this with `PyNeb` (Luridiana et al. 2015), finding an electron temperature $T_e = 16755^{+888}_{-1001}$ K and density $n_e = 2440^{+48}_{-58}$ cm^{-3}. The final measurements are found in Table 1.

We further measure the abundance of the main metals in our galaxy. We use `Pyneb` to infer these quantities. We measured the oxygen abundance with the direct method using [O III]λ5008and [O II]$\lambda\lambda$3727,3730. We find an oxygen abundance of $12 + \log(\mathrm{O/H}) = 7.95 \pm 0.06$. We also detect [N II]$\lambda\lambda$6550,6585, therefore we convert the $T_e(O^{+2})$ to $T_e(O^{+})$ from the intermediate Z relationship from Izotov et al. (2006) and infer a nitrogen abundance of $\log(\mathrm{N/H}) = -5.47 \pm 0.05$, assuming $T_e(N^{+}) = T_e(O^{+})$ (e.g. Berg et al. 2021). By comparing [O II]$\lambda\lambda$3727,3730 and [N II]$\lambda\lambda$6550,6585, we infer $\log(\mathrm{N/O}) = -0.75 \pm 0.05$.

Table 1: Measured properties of GLIMPSED-329380.

Property	Units	Value
General properties		
RA	deg	342.22997617
DEC	deg	-44.5103798
μ	—	2.36 ± 0.01
host component		
z_{sys}^{host}	—	6.63784 ± 0.00004
$T_e(O^{+2})$	K	16755^{+888}_{-1001}
$n_e(S^+)$ †	cm^{-3}	2440^{+48}_{-58}
12 + log(O/H)	—	7.95 ± 0.06
log(N/H)	—	−5.47 ± 0.05
log(N/O)	—	−0.75 ± 0.05
$\log(M_\star)$ §	$M_\odot$	8.19 ± 0.22
AGN component		
z_{sys}^{agn}	—	6.64002 ± 0.00002
$T_e(O^{+2})$	K	18338.24 ± 2320.78
$\log n_e(S^+)$	cm^{-3}	3.10 ± 0.58
$\log M_{BH}$ ‡	$M_\odot$	7.01 ± 0.50

Notes. † n_e is computed for a fix [S ii]$\lambda\lambda$6718,6733 ratio. Errors are based on variations with $T_e(O^{+2})$ and are therefore underestimated. ‡ The M_{BH} is measured in Hα from an exponential profile, and is therefore underestimated (See Sect. 3.2.6). This value is de-lensed. § The stellar mass is indirectly measured from the mass-metallicity relationship of (Chemerynska et al. 2024). The mass is de-lensed.

These N/O abundance is slightly higher than typical standard star forming galaxies, but does not reach values observed in N-enhanced galaxies recently observed at high redshift (e.g. Marques-Chaves et al. 2024; Morel et al. 2025). Because of the difficulties to systematically constrain all the outflowing components, in particular for weaker lines, measuring the same quantities for the outflowing gas remains challenging.

3.1.3. Extreme ionised outflow

One of the main point of interest of GLIMPSED-329380, is the extreme ionised outflow observed in strong emission lines, in particular [O iii]. This component is observed in Fig. 4. As shown in Tab. A.1, the broad components in [O iii] have a significant full-width half maximum (FWHM) of the order of ∼740 km $s^{-1}$and ∼5500 km s^{-1}. The latter is extreme and is rarely seen for ionised outflows (e.g. Arribas et al. 2014; Förster Schreiber et al. 2019; Cooper et al. 2025; Nandi et al. 2026). The first broad component is fitted at the same redshift as the narrow component, but the broader one appears slightly blueshifted. Outflowing broad components with $FWHM > 1000$km $s^{-1}$are rarely seen in star-forming galaxies, even in the most powerful starburst (e.g. Amorín et al. 2012, 2024; Marques-Chaves et al. 2025; Crespo Gómez et al. 2025; Zamora et al. 2025), but are more common in AGN-driven outflows (e.g. Manzano-King et al. 2019; Cooper et al. 2025; Bertola et al. 2025). In that framework, GLIMPSED-329380 lies in the most extremes ionised outflows driven by AGNs (See Fig. 11).

The outflowing velocities observed in GLIMPSED-329380 are significant, and stronger than most warm outflows (e.g. Nandi et al. 2026). In order to estimate if this outflow could lead in the quenching of the galaxy (as discussed in Taylor et al. 2026), we need to estimate the mass loading factor, i.e. the ratio between the outflowing mass rate and the star formation rate. For that, we first need to estimate the outflowing ionised mass from the galaxy, for which we use the luminosity to mass relationship from (Colina et al. 1991), with n_e the electron density in cm^{-3} and L([O iii]λ5008) the [O iii]λ5008 luminosity in erg s^{-1}:

$$M_g = \frac{1.21 \times 10^{-33} L([\text{O III}]\lambda 5008)}{n_e} \quad (1)$$

Then, to estimate the mass rate, we use the standard equation (e.g. Álvarez-Márquez et al. 2021) introduced below, which relates the outflowing mass rate with the ionised mass M_g (in $M_\odot$), the maximum outflowing velocity $V_{max} = |\Delta V + 0.5 v_{FWHM}|$ (with ΔV being the velocity difference between the two peaks (e.g. Arribas et al. 2014), the size of the outflow d (in kpc) and a geometrical parameter K to quantify if the galaxy is elongated or circular. In our case, Fig. 3 shows an elongated object, therefore we set $K = 1$ (see Lutz et al. 2020; Álvarez-Márquez et al. 2021). The equation is described as follow:

$$\dot{M}_g = K \frac{M_g V_{max}}{d} \quad (2)$$

Because of the limited morphological information, we use rough estimates of $d = 0.7'' = 2.46$kpc (de-lensed) , corresponding to the size of the outflow in the 2D spectrum. We compute the mass loading factor as the ratio of the outflowing ionised mass rate and the $SFR_{H\alpha}$ estimated from Kennicutt & Evans (2012):

$$\eta = \frac{\dot{M}_g}{SFR_{H\alpha}} = 10^{41.27 - \log L(H\alpha)} \dot{M}_g \quad (3)$$

Using the dust correct line fluxes, we obtain mass loading factors of $\eta = 0.07 \pm 0.01$ for the first outflow and $\eta > 0.10 \pm 0.02$ for the large outflow. Since both values are well below unity, the mass ejected by the AGN is insufficient to counteract star formation within the galaxy, therefore these outflows are unable to quench this galaxy. Note that these mass loading factors are similar to those of the LRD in Cooper et al. (2025), whose object had the fastest ionised outflow of their catalogue, with one of the lowest mass loading factor. Finally, we infer the kinetic energy of the outflows using $\dot{E}_{out} = \frac{1}{2}\dot{M}_g v_{out}^2$ which gives $\dot{E}_{out} = (1.56 \pm 0.26) \times 10^{41}$erg s^{-1} and $\dot{E}_{out} > (1.24 \pm 0.31) \times 10^{43}$erg s^{-1}. For such extreme outflowing velocities, the energy output is rather small. Comparatively, (Bertola et al. 2025) found $\dot{E}_{out} \sim 3.9 \times 10^{45}$erg s^{-1} for an AGN with similar v_{out}. These results show that, despite the fast outflow observed in [O iii], the impact on the galaxy is rather small. A summary of the kinematic properties of the galaxy can be found in Table 2.

Table 2: Kinematic properties of the ionised gas in the host component.

Property	Units	Outflow 0	Outflow 1
v_{out}	km s^{-1}	425.70 ± 15.17	3263.82 ± 295.97
M_g	$10^6 M_\odot$	15.41 ± 2.23	> 2.72 ± 0.40
$\dot{M}_g$	$M_\odot yr^{-1}$	2.73 ± 0.41	> 3.70 ± 0.64
η	—	0.07 ± 0.01	> 0.10 ± 0.02
$\dot{E}_{out}$	10^{41} erg s^{-1}	1.56 ± 0.26	> 124.06 ± 31.00

Notes. The properties are corrected for dust attenuation.

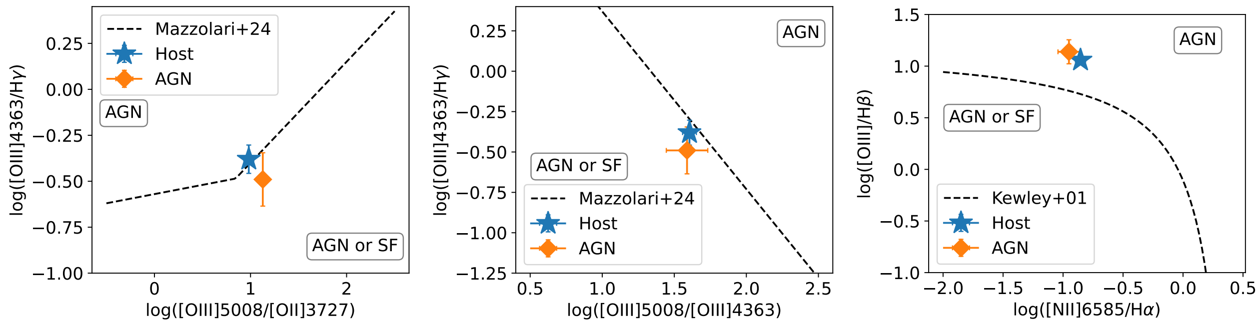

Fig. 6: Lines diagnostic figures for GLIMPSED-329380. Measurements are performed on the narrow lines of both the AGN and host components. Left and center: diagnostics based on [O iii]λ4363 from Mazzolari et al. (2024). Right: BPT diagnostics from Kewley et al. (2001) showing high compatibility with an AGN. [O iii] corresponds to the sum of [O iii]$\lambda\lambda$4960,5008.

We finally note the outflow is also visible in the AGN comment. While slower and less significant, it is observed in [O iii] and Hα as well. This is most probably due to contamination of the AGN spectrum with the host galaxy. We further note that the line profile from [O iii]λ5008 in the AGN is complex and cannot be explained by simple Gaussians. We will now discuss the properties of the AGN.

3.2. AGN properties

3.2.1. Empirical evidence for an AGN

We identified this component as an AGN based on multiple signatures. First, the Hα profile is compatible with a Type-1 AGN BLR. Then, as shown in Fig. 6, GLIMPSED-329380 is clearly identified as an AGN in a BPT diagram (Baldwin et al. 1981; Kewley et al. 2001) and more recent AGN line diagnostics (Mazzolari et al. 2024). Finally, we also note the massive outflows observed in the host, which is most probably produced by an AGN (See Fig. 11). We will therefore assume that we are observing an AGN, and in the following subsections, we will discuss its observed characteristics. Furthermore, we will show that GLIMPSED-329380 also strongly resembles LRDs. The main inferred properties are listed in Table 1.

3.2.2. Black hole mass

In this subsection, we first make the assumption that the observed exponential wings in Hα and Hβ are solely due to gas motion because of the black hole. However, we then discuss that the estimations used here most probably do not translate well to GLIMPSED-329380. Nonetheless, they provide interesting anchor points for comparison with other objects.

We estimate the black hole mass $M_{\rm BH}$ following Reines & Volonteri (2015), which use the single-epoch viral mass estimator from Reines et al. (2013) and an estimated scale factor $\epsilon = 1.075$. This estimator uses the FWHM from the Gaussian fit of Hα. However, as seen earlier, our Hα profile is better fitted by an exponential profile, which has narrower FWHM, leading to an underestimation of the mass. Nonetheless, we obtain a de-lensed black hole mass $\log(M_{\rm BH}/M_\odot) = 7.01 \pm 0.50$. Due to the lack of photometric constraints, we cannot directly measure the stellar mass $M_\star$ of GLIMPSED-329380. However, using the average mass-metallicity calibration at $z = 6 - 8$ from Chemerynska et al. (2024) and the metallicity of the host determined above, we estimate a de-lensed host stellar mass of $\log(M_\star/M_\odot) = 8.19 \pm 0.22$. This stellar mass is low for a system hosting such a massive black hole. For example, applying the local scaling relations from Reines & Volonteri (2015) would predict a black hole mass 2–3 orders of magnitude lower than measured. However, GLIMPSED-329380 aligns well with the behaviour of the LRD population (Jones et al. 2025), which typically shows higher black hole mass to stellar mass ratio, compared to more standard AGNs.

The black hole mass estimates rely on the assumption that the broadening of Hα is driven exclusively by gas motion. However, this assumption may not apply to LRDs. While some studies argue that the observed exponential line profiles in LRDs could still arise from gas motion in stratified BLR clouds (e.g. Scholtz et al. 2026), others attribute these profiles to electron scattering due to extreme densities in the BLR, which would also produce an exponential shape (e.g. Kokorev et al. 2025; Rusakov et al. 2026; Chang et al. 2026). In the latter scenario, the black hole mass estimates would be invalid, as the line broadening would not reflect gas kinematics (e.g. Naidu et al. 2025; de Graaff et al. 2025b).

3.2.3. Electron temperature, electron density, abundances of AGN component and obscuration

In order to characterise the gas surrounding the AGN, we apply a similar analysis as for the host component. We use [O iii]λ5008 and [O iii]λ4363 to measure $T_e(O^{+2})$, and [S ii]$\lambda\lambda$6718,6733 for $n_e(S^+)$. Contrary to the host component, we do not expect to observe a broadening of [S ii]. As the broadening is caused by the BLR, and that high densities are expected in that region, [S ii] might be affected by collisional de-excitation (e.g. Kewley et al. 2019) and is only produced in the narrow line region. We use Pyneb to compute these quantities, and fit them to obtain a coherent solutions. We measure slightly higher electron temperature $T_e(O^{+2}) = 18338 \pm 2321$K than the host, but similar electron densities $\log(n_e(S^+)/\text{cm}^{-3}) = 3.10 \pm 0.58$.

Finally, our model enables us to compute the Balmer decrement for the modeled total flux of Hα and Hβ. We obtain Hα/Hβ = 10.44 ± 3.27. This value is extreme compared to lower redshift AGNs and bright quasi-star objects (QSOs) (e.g. Sun et al. 2026), but typically observed in LRDs (e.g. Torralba et al. 2025; de Graaff et al. 2025b). If caused by dust, it would correspond to an extreme attenuation (e.g. Kocevski et al. 2023). However, the absence of infrared dust re-emission in LRDs seems to largely rule out this explanation (e.g. Casey et al. 2025; Setton et al. 2025), and the high Balmer decrement is probably caused by resonant and/or electron scattering (e.g.

Naidu et al. 2025; de Graaff et al. 2025b; Chang et al. 2026; Rusakov et al. 2026; Chang et al. 2026).

3.2.4. A forest of Fe II lines

One of the feature of our AGN component is the plethora of restframe optical [Fe II] lines detected. Figures 5 and 10 show the fits for these emission lines, and their fluxes are listed in Table A.3. While weak, several of these lines are detected at $> 3\sigma$: [Fe II]λ4245, [Fe II]λ4287, [Fe II]λ4414, [Fe II]λ5159 and [Fe II]λ5263. So far, this [Fe II] forest has only been observed in a few LRDs, such as in local analogues (Ji et al. 2026; Lin et al. 2026) and at high redshifts (Lambrides et al. 2025; D'Eugenio et al. 2025; Torralba et al. 2025). These lines are typically very weak, requiring thus high resolution and deep observations to be properly detected.

We further note that the [Fe II]λ5159 line is blended with the higher level [Fe VII]λ5160 line. This degeneracy between the two blended line was observed and discuss in previous AGNs or LRDs studies (e.g. D'Eugenio et al. 2025; Wang et al. 2025; Lambrides et al. 2025). For the same reason as in *Irony* (D'Eugenio et al. 2025), we believe this emission line to be [Fe II] rather than [Fe VII]: we observe the same [Fe II] forest, and we do not detect He IIλ4686 in the AGN component. Since the ionization potential of He^+ (54 eV) is lower than that of Fe^{+6} (99 eV), we would expect to see He IIλ4686 if [Fe VII]λ5160 was present, which is, however, not the case.

3.2.5. Inflowing gas

In addition to emission lines, the AGN spectrum exhibits an absorption feature at the expected position of Na I (Figure 7), which has also been reported in a few LRDs. Although not as deep as in some previously observed systems (e.g. Ji et al. 2026; Lin et al. 2026), it is clearly detected in our spectrum. Characterising this feature is, however, challenging, as the Na I profile is likely contaminated by the broad emission from He Iλ5876. In objects such as Ji et al. (2026) (see Fig. 10c), where kinematic signatures are less pronounced, He Iλ5876 and Na I are well separated. In our case, the absorption appears redshifted by $\simeq 280\,\mathrm{km\,s^{-1}}$, which is indicative of inflowing gas toward the AGN along the line of sight. This inflow is also consistent with the inability of the fast outflow to quench the host galaxy, as in addition to the low mass loading factor, agas reservoir inflows toward it.

3.2.6. Balmer break and black body

Due to the limited spectral coverage, we cannot probe the Balmer break with traditional estimators (e.g. D4000). In addition, as described in the method, the spectrum based on the global noise reduction has issues on the edges of the spectrum. Therefore, to probe the Balmer break, we define region, in the NOD difference spectrum of the AGN component, which does not suffer from the same sky background issue. In order to avoid edge noise and emission lines, we define the blue region as 27 960 – 28 400Å (observed, rest-frame 3660 – 3717Å), and the red region as 28 660 – 29 490Å (observed, rest-frame 3751 – 3860Å. We then measure the average flux in these two regions and obtain a Balmer break $BB = 1.82 \pm 0.39$, shown in Fig. 8. This result is significant and is compatible with previous observations of LRD (e.g. de Graaff et al. 2025b).

In additional, previous studies also observed that black body models fit well LRDs (e.g. Naidu et al. 2025; de Graaff et al.

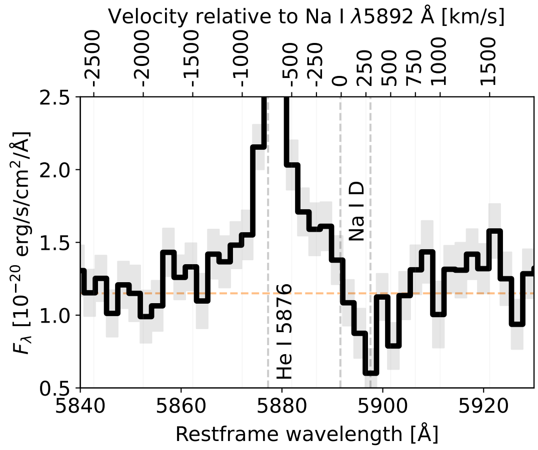

Fig. 7: Na I D absorption feature in the AGN component with top axis centered around the Na Iλ5890line.

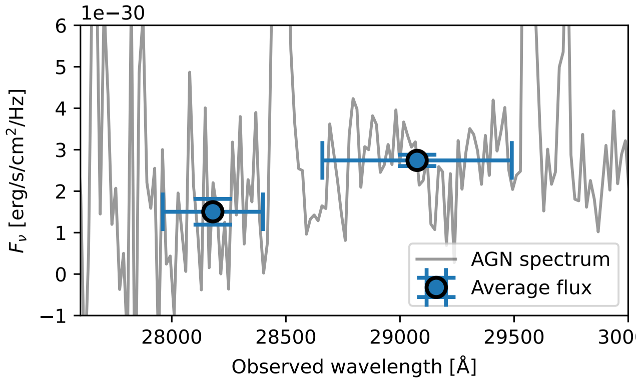

Fig. 8: Balmer break of the AGN component in the NOD difference reduced spectrum

2025b; Sun et al. 2026), calling this model the black hole star (BH*, Naidu et al. 2025). To test this, we define two simple models, the standard black body (BB, e.g. Naidu et al. 2025; Sun et al. 2026) and the modified black body (MBB, following de Graaff et al. 2025b) which includes an additional component to account for the contribution of the galaxy. These models are defined by three parameters, the temperature T, the scaling factor A and the slope β, which is set to $\beta = 0$ for the BB model. Following (de Graaff et al. 2025b), we define our models as the following:

$$f_\nu = A \times B_\nu(T) \times \left(\frac{5500\text{Å}}{\lambda}\right)^\beta \tag{4}$$

where λ is the restframe wavelength in Å and $B_\nu(T)$ the general definition of the black body spectrum. We fit these two models to our AGN component (NOD difference spectrum with emission lines masked) and show it in Fig. 9. We first note that, while the BB model is well parametrised, the MBB model does suffer from degeneracies between the scale A and slope β. Nonetheless, the reduced χ^2 and the information criteria are similar between the two parametrisation. The models have a temperature between $T \sim 4000 - 5000$K, which is comparable to the previous observations (de Graaff et al. 2025b; Sun et al. 2026). The resulting bolometric luminosities of $L_{\mathrm{blackbody}} \sim 10^{45}\mathrm{erg\,s^{-1}}$ are

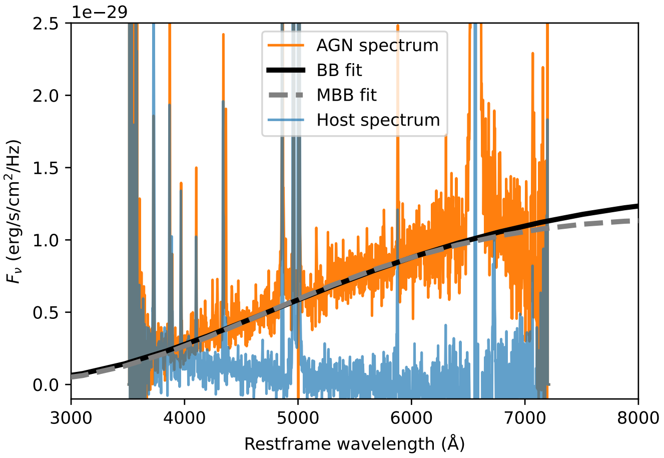

Fig. 9: Fit of the AGN component with a simple black body (BB, following Naidu et al. 2025; Sun et al. 2026) and a modified black body (MBB, following de Graaff et al. 2025b). We also report the host component as a comparison.

Table 3: Black bodies fitting parameters for the AGN component

Parameters	Units	Black Body	Modified Black Body
T	K	5064.73 ± 46.08	4152.19 ± 349.45
A	10^{25}	2.28 ± 0.11	7.20 ± 3.85
β	—	$0^\dagger$	1.17 ± 0.55
χ^2_ν	—	1.09	1.09
BIC	—	85.80	87.66
AIC	—	76.38	73.53
$L_{\rm blackbody}$	10^{45} erg s^{-1}	1.37 ± 0.05	1.12 ± 0.91

Notes. T is the black body temperature, A is the de-lensed scaling factor (including the conversion for steradians), β is the slope modifier for the modified black body, χ^2_ν is the reduced χ^2, BIC and AIC are the Bayesian and Akaike information criteria. $L_{\rm blackbody}$ is the de-lensed bolometric luminosity of the models. † β is fixed to 0 for the standard black body

on the higher end of previously observed LRDs (de Graaff et al. 2025b), but are compatible with their results. This difference might be explained by the lack of spectral coverage red-ward of Hα. Our AGN component therefore matches well with the LRD population. The fitted parameters can be found in Table 3.

4. Discussion

4.1. Similarities with little red dots

LRDs likely constitute a diverse population of compact extragalactic sources that do not all exhibit the same spectral properties. Nevertheless, several common characteristics appear to emerge: a V-shaped continuum, prominent broad wings in the Balmer lines, a strong absorption feature around $\sim$ 4550 Å, and the presence of [Fe II] emission (e.g. Matthee et al. 2024; Furtak et al. 2024; Greene et al. 2024; Juodžbalis et al. 2024; D'Eugenio et al. 2025; Kokorev et al. 2025; Pérez-González et al. 2026; Ji et al. 2026). GLIMPSED-329380 shows multiple features in common with typical LRDs. We will now discuss these different features. To illustrate it, we compare the spectrum of GLIMPSED-329380 with those of two well-studied LRDs in Fig. 10, the Lord of LRDs from Ji et al. (2026), a low redshift ($z \sim 0.1$) LRD, and the AGN Rosetta Stone from Juodžbalis et al. (2024) at $z \sim 2.26$. The three spectra have comparable signal-to-noise and spectral resolution.

One of the initial criteria for LRD was the overall shape of the SED, a "V-shaped" SED (e.g. Matthee et al. 2024). By fitting our AGN component (NOD difference) with $f_\lambda \sim \lambda^{\beta_{\rm opt}}$, we obtain a positive slope $\beta_{\rm opt} = 0.37 \pm 0.05$. Using F125W and F160W from the HST photometry (excluding F105W, which might include Lyman-α), we can approximate the UV slope from F125W and F160W HST filters: $\beta_{\rm UV} = -1.60 \pm 0.04$. These slopes match well the "V-shape" description and sets our galaxy in the category of LRDs (e.g. Brazzini et al. 2026). In addition, recent papers highlighted the black body shape of LRDs (e.g. de Graaff et al. 2025b; Naidu et al. 2025; Sun et al. 2026) which is well reproduced in our AGN component (see Sect. 3.2.6), and our temperatures of $T = 4000 - 5000$K compare well to other LRDs (e.g. de Graaff et al. 2025b). Our observations of a Balmer-break also reinforces the comparison. Furthermore, the limited Spitzer data points enable us to tentatively exclude a red AGN (e.g. Fei et al. 2026) due to the non-detection of the IRAC3 and 4 bands, as these objects are expected to shine in the restframe infrared, and not drop like LRDs (e.g. de Graaff et al. 2025b). Therefore, the general morphology of our objects fits well the typical LRD.

Another striking feature is the presence of the absorption feature around $\sim$ 4550 Å (see panel a) in Fig. 10), which appears in many individual LRDs and in deep stacks (Pérez-González et al. 2026). A plausible explanation would be metallic absorption from permitted Fe II lines (Pérez-González et al. 2026), as many of these lines are identified around $\sim$ 4550Å (e.g. Kovačević et al. 2010; Kovačević-Dojčinović et al. 2025).

We also report the presence of numerous [Fe II] emission lines, which are typically observed in LRDs spectra of sufficient depth and spectral resolution (e.g. Juodžbalis et al. 2024; D'Eugenio et al. 2025; Lambrides et al. 2025; Ji et al. 2026; Lin et al. 2026). These requirements make it difficult to observe these lines at higher redshift, explaining the low number of detections in these galaxies (Lambrides et al. 2025; D'Eugenio et al. 2025). GLIMPSED-329380 is one of these few high redshift ($z \sim 6.64$) objects with significant detections of multiple [Fe II] lines, as discussed earlier (Sect. 3.2.4).

Finally, we also observe exponential wings in the Hα emission line (see Sect. 2.4), as shown by the triangular-shaped Hα profile in panel e) of Fig. 10. This is comparable to some LRDs (e.g. Rusakov et al. 2026), including the Rosetta Stone and the Lord of LRDs. In Hβ, this exponential profile is not as strong due to the strong Balmer decrement and the stronger contribution of the narrow Hβ component to the emergent line profile. Furthermore, we note the absence of clear Balmer absorption in the BLR of Hα and Hβ that are clearly shown in the Rosetta Stone and Lord of LRDs. These absorption features are only expected in extreme densities, but depend on the complex conditions of the gas and the contribution of the narrow emissions from the underlying component, therefore many configurations of the absorption are observed (e.g. Juodžbalis et al. 2024; Ji et al. 2025; D'Eugenio et al. 2025; Lambrides et al. 2025; Ji et al. 2026; Lin et al. 2026; Rusakov et al. 2026), including no visible absorption (e.g Rusakov et al. 2026). This absence of absorption can easily be explained in the situation where the absorption is at the systematic redshift. In that case, it would be compensated by the narrow component, which might be the case in our situation. Such absorption at high densities were also observed in He I

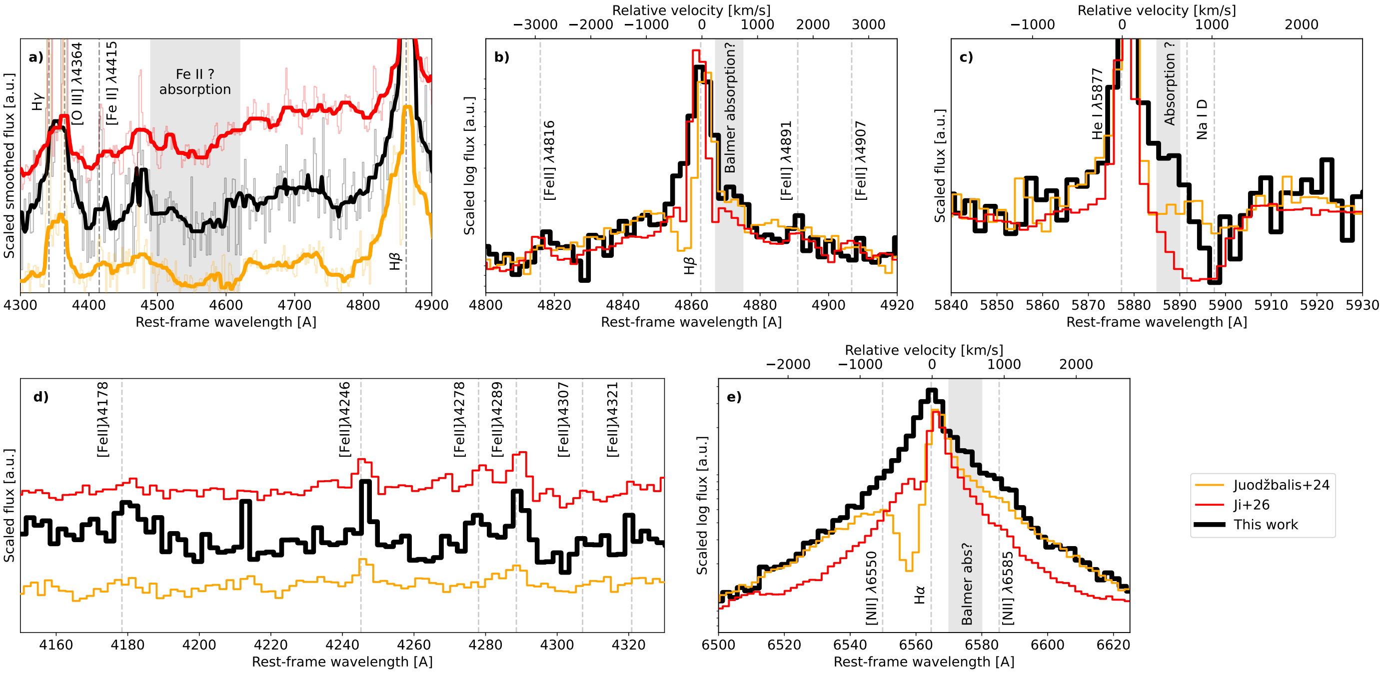

Fig. 10: Comparison between the LRD-like features the AGN component of GLIMPSED-329380and (Ji et al. 2026) and (Juodžbalis et al. 2024). The fluxes are scaled: a) shows the Fe II absorption forest b) Hβ in log-scale c) He Iλ5875 and Na I D complex d) the blue part of the [Fe II] forest, and e) Hα in log-scale.

(e.g. Kokorev et al. 2025). However, we note that, while we do not observe clear absorption features in Hα, Hβ, and He I, we observe some surprising common behaviour. In Hβ and He Iλ5877, we observe a sharp drop of the profile at $\sim$ 500 km s^{-1}, with a red-ward small absorption, possibly indicating a common origin. This exact feature is not visible in Hα, but we note that the red wing of Hα does also have a sharp drop around the same relative velocity. In the end, all these possible absorptions are very tentative. They require higher resolution observations to be properly analysed, and do not represent concluding arguments in favour of an LRD.

While our objects lack NIRCam observations and rest-frame UV spectra, their strong similarities to typical LRDs reinforce the likelihood that they belong to the same class of objects. We will now discuss the implications of this source being an LRD.

4.2. Nature of the ionised outflow in GLIMPSED-329380

The frequency of ionised outflows in LRDs remains poorly constrained, as most have been observed with low-resolution spectroscopy (e.g. PRISM) or at higher resolution but with low signal-to-noise (e.g. Matthee et al. 2024). So far, ionised outflows have only rarely been detected, in LRDs observed with both higher resolution and sufficient signal-to-noise (Cooper et al. 2025; Chen et al. 2026; D'Eugenio et al. 2026). While theoretical models predict that outflows may be trapped within the dense gas envelope surrounding LRDs and re-emitted as black body radiation (Kido et al. 2025), their detection in some systems may suggest that the envelope is at least partially clumpy or has been disrupted, allowing a fraction of the gas to escape. Interestingly, the extreme outflow of GLIMPSED-329380 is contrasted by its minor impact on the galaxy. Indeed, measurements of the mass loading factor and kinetic energy from the outflowing and inflowing gas show a minimal impact, much smaller than other outflows with comparable velocities (e.g. Bertola et al. 2025). This reinforces the argument for a disrupted envelope, which would only release a tiny fraction of the gas.

Figure 11 shows the maximum outflowing velocity, $v_{\rm out}$, against the total Hα luminosity of GLIMPSED-329380, compared to observations of star-forming galaxies, AGN, and LRDs. In this context, GLIMPSED-329380 stands out as a clear outlier due to its extreme outflow velocity. Such high-velocity outflows are observed almost exclusively in AGN-dominated systems and are significantly stronger than those typically found in star-forming galaxies, including even the most extreme starbursts (e.g., Álvarez-Márquez et al. 2021; Rodríguez Del Pino et al. 2026). The LRDs presented by Chen et al. (2026) and D'Eugenio et al. (2026) also lie within the AGN-dominated region of the diagram. Although the current sample of LRDs with detected outflows remains limited, their location in this parameter space strongly supports an AGN-driven origin.

In conclusion, we found strong evidence that the observed fast ionised outflow in GLIMPSED-329380 is driven by AGN activity. The similarities between this object and the diverse class of LRDs, including spectral features, emission line profiles, and continuum shape, suggest that this LRD hosts an active AGN. To date, most LRD studies have relied on low-resolution PRISM data, which may limit the detection of outflows. Future medium- or high-resolution spectroscopic observations of LRDs will be important to determine whether such extreme outflows are a common feature of these systems.

5. Summary and conclusion

In this work, we present GLIMPSED-329380, a z = 6.64 galaxy behind the Abell S1063 cluster, observed as part of the deep JWST/NIRSpec GLIMPSE-D survey. This galaxy stands out due to its spatially resolved structure showing a compact AGN com-

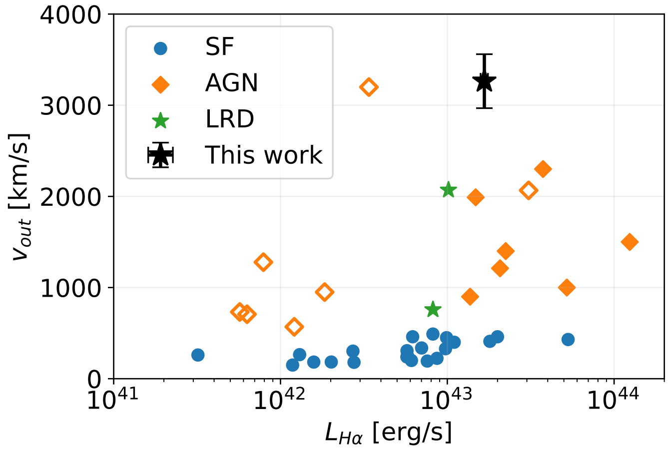

Fig. 11: Comparison between the outflowing velocities and total Hα flux from star formation (SF) feedback (Förster Schreiber et al. 2019; Llerena et al. 2023; Saldana-Lopez et al. 2025), AGN feedback (Förster Schreiber et al. 2019; Übler et al. 2023; Bertola et al. 2025) (where Bertola et al. (2025) includes an outflow at > 3000km s^{-1}) and for the few detected outflowing LRDs (D'Eugenio et al. 2026; Chen et al. 2026). The full markers show the total Hα, while empty markers correspond to the broad components only.

ponent exhibiting classic LRD features, and an extended host galaxy exhibiting a very fast ionised outflow driven by the AGN. Using medium-resolution spectroscopy, we separated the spectra of the AGN and host, revealing a wealth of emission and absorption features. The main results from their analysis are the following:

- The spectrum of the host galaxy exhibits an extreme ionised outflow, mainly observed in [O III]$\lambda\lambda$4960,5008, Hα and Hβ. This outflow is modelled with two components with maximal outflowing velocities of $v_{\rm out}$ ∼ 425km s^{-1} and $v_{\rm out}$ ∼ 3263km s^{-1} respectfully. The first outflow is observed at approximately the same redshift as the narrow component, but the second outflow is blueshifted by Δz ∼ 0.01. The narrow component is compatible with no dust attenuation, while the two outflowing components are compatible with some attenuation, hinting for expulsion of dust with the outflow. Despite the high velocity of one outflowing component, the observed outflows are not significant for the galaxy, as the mass loading factors reach ∼ 7% and > 10% and the inferred kinetic energy is rather low compared to similar velocities AGN-driven outflows (Bertola et al. 2025). The gas in the host component shows a relatively low oxygen abundance of $12 + \log(O/H) \sim 7.95$ and slight nitrogen enhancements $\log(N/O) \sim -0.75$. Using a mass-metallicity relationship (Chemerynska et al. 2024), we estimate a de-lensed stellar mass of $\log(M_\star/M_\odot) \sim 8.2$.
- The AGN component shows many typical features of LRDs. First, we observe the V-shaped SED. Then, large exponential wings in Hα, which are significantly weaker in Hβ. The Balmer decrement is too large to be explained by dust attenuation, and is most probably caused by electron scattering instead. We infer a significant over-massive black hole mass, whose ratio with the stellar mass of the host places it 2-3 orders of magnitude higher than typical relationship (Reines & Volonteri 2015), well in-line with typical LRD population (Jones et al. 2025). GLIMPSED-329380 further displays multiple significant detections of forbidden [Fe II] lines, which are only observed in LRD with reasonable exposure time and resolution. The rest-frame optical continuum is also well fitted by a black body, as earlier observed in other LRDs (de Graaff et al. 2025b). The significant absorption observed around ∼ 4550 Å restframe in the AGN spectrum is also a common feature of LRDs. Together, these features providing strong evidence that GLIMPSED-329380 hosts an LRD.

Only a few LRDs have detected outflows, likely due to the low resolution or shallow depth of most spectra. In these cases, the extreme velocities are only consistent with AGN-driven outflows, providing compelling evidence that LRDs host AGNs. However, the current statistical sample of outflowing LRDs remains too small to generalise to the broader LRD population. With its extreme outflow and detailed spectral features, GLIMPSED-329380 offers a unique opportunity to probe LRDs in a regime that has, until now, been largely unexplored.

Acknowledgements. DK would like to thank Ilona Morel for the help with Pyneb. HA acknowledges support from CNES, focused on the JWST mission, and the Programme National Cosmology and Galaxies (PNCG) of CNRS/INSU with INP and IN2P3, co-funded by CEA and CNES and from the French National Research Agency (ANR) under grant ANR-21-CE31-0838. This work is based [in part] on observations made with the NASA/ESA/CSA James Webb Space Telescope. The data were obtained from the Mikulski Archive for Space Telescopes at the Space Telescope Science Institute, which is operated by the Association of Universities for Research in Astronomy, Inc., under NASA contract NAS 5-03127 for JWST. These observations are associated with program #9223.
Softwares: LMFit (Newville et al. 2025), Astropy (Collaboration et al. 2022), Numpy (Harris et al. 2020), Matplotlib (Hunter 2007), Scipy (Virtanen et al. 2020), msaexp (Brammer 2023).

References

Álvarez-Márquez, J., Marques-Chaves, R., Colina, L., & Pérez-Fournon, I. 2021, A&A, 647, A133
Amorín, R., Vílchez, J. M., Hägele, G. F., et al. 2012, ApJ, 754, L22
Amorín, R. O., Rodríguez-Henríquez, M., Fernández, V., et al. 2024, A&A, 682, L25
Arribas, S., Colina, L., Bellocchi, E., Maiolino, R., & Villar-Martín, M. 2014, A&A, 568, A14
Atek, H., Chisholm, J., Kokorev, V., et al. 2025, arXiv e-prints, arXiv:2511.07542
Baldwin, J. A., Phillips, M. M., & Terlevich, R. 1981, PASP, 93, 5
Berg, D. A., Chisholm, J., Erb, D. K., et al. 2021, ApJ, 922, 170
Bertola, E., Cresci, G., Venturi, G., et al. 2025, A&A, 699, A220
Brammer, G. 2023, msaexp: NIRSpec analyis tools
Brammer, G. B., Marchesini, D., Labbé, I., et al. 2016, ApJS, 226, 6
Brazzini, M., D'Eugenio, F., Maiolino, R., et al. 2026, arXiv e-prints, arXiv:2601.22214
Cardelli, J. A., Clayton, G. C., & Mathis, J. S. 1989, ApJ, 345, 245
Casey, C. M., Akins, H. B., Finkelstein, S. L., et al. 2025, ApJ, 990, L61
Chang, S.-J., Gronke, M., Matthee, J., & Mason, C. 2026, MNRAS, 545, staf2131
Chemerynska, I., Atek, H., Dayal, P., et al. 2024, ApJ, 976, L15
Chen, X., Ichikawa, K., Akiyama, M., et al. 2026, ApJ, 999, 30
Colina, L., Sparks, W. B., & Macchetto, F. 1991, ApJ, 370, 102
Collaboration, A., Price-Whelan, A. M., Lim, P. L., et al. 2022, ApJ, 935, 167
Cooper, R. A., Caputi, K. I., Iani, E., et al. 2025, ApJ, 994, 102
Crespo Gómez, A., Tamura, Y., Colina, L., et al. 2025, arXiv e-prints, arXiv:2511.14658
de Graaff, A., Brammer, G., Weibel, A., et al. 2025a, A&A, 697, A189
de Graaff, A., Hviding, R. E., Naidu, R. P., et al. 2025b, arXiv e-prints, arXiv:2511.21820
D'Eugenio, F., Juodžbalis, I., Ji, X., et al. 2026, MNRAS, 545, staf2117
D'Eugenio, F., Nelson, E., Ji, X., et al. 2025, arXiv e-prints, arXiv:2510.00101
Endsley, R., Stark, D. P., Whitler, L., et al. 2024, MNRAS, 533, 1111
Fei, Q., Fujimoto, S., Brammer, G., et al. 2026, arXiv e-prints, arXiv:2602.12325
Förster Schreiber, N. M., Übler, H., Davies, R. L., et al. 2019, ApJ, 875, 21

Fujimoto, S., Asada, Y., Naidu, R. P., et al. 2025, arXiv e-prints, arXiv:2512.11790
Furtak, L. J., Labbé, I., Zitrin, A., et al. 2024, Nature, 628, 57
Greene, J. E., Labbe, I., Goulding, A. D., et al. 2024, ApJ, 964, 39
Harris, C. R., Millman, K. J., van der Walt, S. J., et al. 2020, Nature, 585, 357
Hopkins, P. F., Kereš, D., Oñorbe, J., et al. 2014, MNRAS, 445, 581
Hunter, J. D. 2007, Computing in Science & Engineering, 9, 90
Inayoshi, K. & Maiolino, R. 2025, ApJ, 980, L27
Izotov, Y. I., Stasińska, G., Meynet, G., Guseva, N. G., & Thuan, T. X. 2006, A&A, 448, 955
Ji, X., D'Eugenio, F., Juodžbalis, I., et al. 2026, MNRAS, 545, staf2235
Ji, X., Maiolino, R., Übler, H., et al. 2025, MNRAS, 544, 3900
Jones, B. L., Kocevski, D. D., Pacucci, F., et al. 2025, arXiv e-prints, arXiv:2510.07376
Juodžbalis, I., Ji, X., Maiolino, R., et al. 2024, MNRAS, 535, 853
Kennicutt, R. C. & Evans, N. J. 2012, ARA&A, 50, 531
Kewley, L. J., Dopita, M. A., Sutherland, R. S., Heisler, C. A., & Trevena, J. 2001, ApJ, 556, 121
Kewley, L. J., Nicholls, D. C., Sutherland, R., et al. 2019, ApJ, 880, 16
Kido, D., Ioka, K., Hotokezaka, K., Inayoshi, K., & Irwin, C. M. 2025, MNRAS, 544, 3407
King, A. & Pounds, K. 2015, ARA&A, 53, 115
Kocevski, D. D., Onoue, M., Inayoshi, K., et al. 2023, ApJ, 954, L4
Kokorev, V., Chisholm, J., Naidu, R. P., et al. 2025, arXiv e-prints, arXiv:2511.07515
Kovačević, J., Popović, L. Č., & Dimitrijević, M. S. 2010, ApJS, 189, 15
Kovačević-Dojčinović, J., Dojčinović, I., Lakićević, M., & Popović, L. Č. 2025, A&A, 694, A289
Lambrides, E., Larson, R., Hutchison, T., et al. 2025, arXiv e-prints, arXiv:2509.09607
Lin, X., Fan, X., Cai, Z., et al. 2026, ApJ, 997, 364
Llerena, M., Amorín, R., Pentericci, L., et al. 2023, A&A, 676, A53
Luridiana, V., Morisset, C., & Shaw, R. A. 2015, A&A, 573, A42
Lutz, D., Sturm, E., Janssen, A., et al. 2020, A&A, 633, A134
Manzano-King, C. M., Canalizo, G., & Sales, L. V. 2019, ApJ, 884, 54
Marques-Chaves, R., Schaerer, D., Dessauges-Zavadsky, M., et al. 2025, arXiv e-prints, arXiv:2510.12411
Marques-Chaves, R., Schaerer, D., Kuruvanthodi, A., et al. 2024, A&A, 681, A30
Matthee, J., Naidu, R. P., Brammer, G., et al. 2024, ApJ, 963, 129
Mazzolari, G., Übler, H., Maiolino, R., et al. 2024, A&A, 691, A345
Morel, I., Schaerer, D., Marques-Chaves, R., et al. 2025, arXiv e-prints, arXiv:2511.20484
Naidu, R. P., Matthee, J., Katz, H., et al. 2025, arXiv e-prints, arXiv:2503.16596
Nandi, P., Colina, L., Riffel, R. A., et al. 2026, arXiv e-prints, arXiv:2602.08447
Newville, M., Otten, R., Nelson, A., et al. 2025, LMFIT: Non-Linear Least-Squares Minimization and Curve-Fitting for Python
Osterbrock, D. E. & Ferland, G. J. 2006, Astrophysics of gaseous nebulae and active galactic nuclei
Pérez-González, P. G., Barro, G., Carniani, S., et al. 2026, arXiv e-prints, arXiv:2602.20247
Reines, A. E., Greene, J. E., & Geha, M. 2013, ApJ, 775, 116
Reines, A. E. & Volonteri, M. 2015, ApJ, 813, 82
Rinaldi, P., Bonaventura, N., Rieke, G. H., et al. 2025, ApJ, 992, 71
Roberts-Borsani, G. W., Saintonge, A., Masters, K. L., & Stark, D. V. 2020, MNRAS, 493, 3081
Rodríguez Del Pino, B., Arribas, S., Perna, M., et al. 2026, arXiv e-prints, arXiv:2601.06255
Rusakov, V., Watson, D., Nikopoulos, G. P., et al. 2026, Nature, 649, 574
Saldana-Lopez, A., Chisholm, J., Gazagnes, S., et al. 2025, MNRAS, 544, 132
Sanders, R. L., Shapley, A. E., Topping, M. W., et al. 2025, arXiv e-prints, arXiv:2508.10099
Scholtz, J., D'Eugenio, F., Maiolino, R., et al. 2026, arXiv e-prints, arXiv:2603.22277
Setton, D. J., Greene, J. E., Spilker, J. S., et al. 2025, ApJ, 991, L10
Steinhardt, C. L., Jauzac, M., Acebron, A., et al. 2020, ApJS, 247, 64
Storey, P. J. & Zeippen, C. J. 2000, MNRAS, 312, 813
Sun, W. Q., Naidu, R. P., Matthee, J., et al. 2026, arXiv e-prints, arXiv:2601.20929
Taylor, A. J., Kokorev, V., Kocevski, D. D., et al. 2025, ApJ, 989, L7
Taylor, E., Carnall, A. C., Maltby, D., et al. 2026, arXiv e-prints, arXiv:2601.02269
Torralba, A., Matthee, J., Pezzulli, G., et al. 2025, arXiv e-prints, arXiv:2510.00103
Übler, H., Maiolino, R., Curtis-Lake, E., et al. 2023, A&A, 677, A145
Veilleux, S., Maiolino, R., Bolatto, A. D., & Aalto, S. 2020, A&A Rev., 28, 2
Virtanen, P., Gommers, R., Oliphant, T. E., et al. 2020, Nature Medicine, 17, 261
Wang, B., Leja, J., Katz, H., et al. 2025, arXiv e-prints, arXiv:2508.18358
Zamora, S., Díaz, A. I., Terlevich, R., Terlevich, E., & Amorín, R. 2025, A&A, 696, A22

Appendix A: Tables of emission lines

In this appendix, we report the tables of emission lines measured in GLIMPSED-329380. In the following table, the first column provides the name of the emission (or absorption) line of interest with its associated rest-frame wavelength. The second column report the FWHM velocity dispersion for the lines and the final column reports the observed (not de-lensed) integrated flux of the line. Table A.1 reports the measurement of the lines in the host component, and Table A.2 reports the emission (and absorption) lines from the AGN, except for the forbidden [Fe II] lines which are reported separately in Table A.3.

Table A.1: host emission line fits.

Line (1)	$v_{\rm FWHM}$ (2) km/s	Flux (3) 10^{-18} cgs
Narrow lines ($z = 6.63784 \pm 0.00004$)		
[O II]λ3727.09	522.01 ± 7.11	4.62 ± 0.54
[O II]λ3729.88	521.62 ± 7.10	3.05 ± 0.51
H$\gamma\lambda$4341.68	448.12 ± 6.10	2.64 ± 0.38
[O III]λ4364.44	445.78 ± 6.07	1.10 ± 0.12
He IIλ4687.02	415.10 ± 5.65	0.31 ± 0.10
H$\beta\lambda$4862.68	400.10 ± 5.45	5.18 ± 0.36
He Iλ4923.304	395.18 ± 5.38	< 0.32
[O III]λ4960.30	392.23 ± 5.34	14.88 ± 0.37
[O III]λ5008.24	388.48 ± 5.29	44.35 ± 1.12
[N II]λ6549.86	297.04 ± 4.04	0.66 ± 0.06
H$\alpha\lambda$6564.61	296.37 ± 4.03	14.07 ± 0.60
[N II]λ6585.27	295.44 ± 4.02	1.97 ± 0.17
He Iλ6679.995	291.25 ± 3.96	0.52 ± 0.15
[S II]λ6718.29	289.59 ± 3.94	< 1.11
[S II]λ6732.67	288.98 ± 3.93	< 0.78
Outflow 0 ($z = 6.63927 \pm 0.00019$)		
H$\gamma\lambda$4341.68	738.65 ± 28.82	1.65 ± 0.49
H$\beta\lambda$4862.68	738.65 ± 28.82	3.32 ± 0.55
[O III]λ4960.30	738.65 ± 28.82	4.43 ± 0.63
[O III]λ5008.24	738.65 ± 28.82	13.34 ± 1.91
H$\alpha\lambda$6564.61	738.65 ± 28.82	14.36 ± 1.23
[S II]λ6718.29	738.65 ± 28.82	< 1.45
[S II]λ6732.67	738.65 ± 28.82	< 1.35
Outflow 1 ($z = 6.62486 \pm 0.00535$)		
H$\beta\lambda$4862.68	5508.81 ± 540.18	< 1.40
[O III]λ4960.30	5508.81 ± 540.18	1.84 ± 0.27
[O III]λ5008.24	5508.81 ± 540.18	5.53 ± 0.80
H$\alpha\lambda$6564.61	5508.81 ± 540.18	4.63 ± 1.00

Notes. (1) Emission line name (2) full width half maximum (FWHM) velocity (3) Observed line flux in cgs=erg s^{-1} cm^{-2}. Low signal-to-noise measurements (< 3) are reported as $< 3\sigma$.

Table A.2: List of emission lines from the AGN component, excluding [Fe II] lines.

Line (1)	$v_{\rm FWHM}$ (2) km/s	Flux (3) 10^{-18} cgs
Narrow lines ($z = 6.64006 \pm 0.00002$)		
[O II]λ3727.09	310.92 ± 3.31	2.04 ± 0.25
[O II]λ3729.88	310.69 ± 3.31	< 0.65
[Ne III]λ3869.86	299.45 ± 3.19	3.48 ± 0.15
He Iλ3889.75	297.92 ± 3.17	0.68 ± 0.12
[Ne III]λ3968.59	292.00 ± 3.11	1.19 ± 0.13
H$\epsilon\lambda$3971.20	291.81 ± 3.11	0.63 ± 0.14
[S II]λ4069.75	284.74 ± 3.03	0.27 ± 0.09
[S II]λ4077.50	284.20 ± 3.03	< 0.28
H$\delta\lambda$4102.89	282.44 ± 3.01	1.02 ± 0.09
H$\gamma\lambda$4341.68	266.91 ± 2.84	2.19 ± 0.10
[O III]λ4364.44	265.51 ± 2.83	0.71 ± 0.23
He Iλ4472.735	259.09 ± 2.76	0.21 ± 0.07
[Ar IV]λ4713.57	245.85 ± 2.62	< 0.21
[Ar IV]λ4741.49	244.40 ± 2.60	< 0.21
H$\beta\lambda$4862.68	238.31 ± 2.54	2.66 ± 0.71
He Iλ4923.304	235.37 ± 2.51	< 0.22
[O III]λ4960.30	233.62 ± 2.49	9.20 ± 0.14
[O III]λ5008.24	231.38 ± 2.46	27.42 ± 0.42
He Iλ5017.42	230.96 ± 2.46	0.39 ± 0.09
[N II]λ5756.24	201.32 ± 2.14	< 0.23
He Iλ5877.249	197.17 ± 2.10	0.83 ± 0.09
Na Iλ5891.58	196.69 ± 2.09	> -0.23
Na Iλ5897.56	196.49 ± 2.09	-0.28 ± 0.08
[O I]λ6302.05	183.88 ± 1.96	0.29 ± 0.08
[N II]λ6549.86	176.92 ± 1.88	0.27 ± 0.06
H$\alpha\lambda$6564.61	176.53 ± 1.88	7.18 ± 0.36
[N II]λ6585.27	175.97 ± 1.87	0.80 ± 0.16
He Iλ6679.995	173.48 ± 1.85	0.44 ± 0.11
[S II]λ6718.29	172.49 ± 1.84	0.34 ± 0.10
[S II]λ6732.67	172.12 ± 1.83	0.35 ± 0.10
BLR ($z = 6.64006 \pm 0.00002$)†		
H$\beta\lambda$4862.68	1013.83 ± 20.19	6.87 ± 0.35
H$\alpha\lambda$6564.61	1013.83 ± 20.19	83.88 ± 3.05
Outflow ($z = 6.63841 \pm 0.00023$)		
[O III]λ4364.44	602.61 ± 26.61	1.62 ± 0.41
[O III]λ4960.30	602.61 ± 26.61	2.13 ± 0.24
[O III]λ5008.24	602.61 ± 26.61	6.42 ± 0.71
H$\alpha\lambda$6564.61	602.61 ± 26.61	8.41 ± 1.19

Notes. (1) Line name including the vacuum wavelength (2) line FWHM velocity (3) Observed line flux in cgs=erg s^{-1} cm^{-2}. Low signal-to-noise measurements (< 3) are reported as $< 3\sigma$. † the BLR is exponential, therefore the FWHM is measured differently with $v_{\rm FWHM} = 2s \ln 2 c\lambda^{-1}$

Table A.3: [Fe II] emission line forest in the AGN component

Line (1)	v_{FWHM} (2) km/s	Flux (3) 10^{-18} cgs
[Fe II]λ4178.38	277.34 ± 2.95	< 0.28
[Fe II]λ4246.01	272.92 ± 2.91	0.35 ± 0.08
[Fe II]λ4278.04	270.88 ± 2.88	< 0.25
[Fe II]λ4288.60	270.21 ± 2.88	0.36 ± 0.08
[Fe II]λ4307.11	269.05 ± 2.86	< 0.22
[Fe II]λ4320.84	268.19 ± 2.86	< 0.23
[Fe II]λ4359.59	265.81 ± 2.83	< 0.43
[Fe II]λ4415.02	262.47 ± 2.79	0.29 ± 0.08
[Fe II]λ4815.89	240.62 ± 2.56	< 0.22
[Fe II]λ4890.99	236.93 ± 2.52	< 0.22
[Fe II]λ4906.72	236.17 ± 2.51	< 0.21
[Fe II]λ5044.93	229.70 ± 2.45	< 0.20
[Fe II]λ5160.23	224.57 ± 2.39	0.38 ± 0.07
[Fe II]λ5263.10	220.18 ± 2.34	0.21 ± 0.07
[Fe II]λ5274.83	219.69 ± 2.34	< 0.21

Notes. (1) emission lines with associated vacuum wavelength (2) FWHM velocity (3) Flux in cgs = erg s^{-1} cm^{-2}. Low signal-to-noise measurements (< 3) are reported as $<3\sigma$.